Article

Small persistent humid forest clearings drive tropical forest biomass losses

https://doi.org/10.1038/s41586-025-09870-7

Received: 8 January 2025

Accepted: 5 November 2025

Published online: 7 January 2026

Check for updates

Yidi Xu[1], Philippe Ciais[1]✉, Maurizio Santoro[2], Clément Bourgoin[3], François Ritter[1,4], Agnès Pellissier-Tanon[1], Yu Feng[1,5], Chuanlong Zhou[1], Guojin He[6], Viola Heinrich[7,8], Simon Besnard[7], Nathaniel Robinson[9], Susan C. Cook-Patton[10], Jérôme Chave[11], Luiz E. O. C. Aragao[12,13], Jean P. Ometto[12], Simon P. K. Bowring[1], Ibrahim Fayad[1], Lei Zhu[14], Yang Su[1,15], Jean-Pierre Wigneron[16] & Wei Li[14]✉

Tropical forests store about half of the global forest aboveground carbon (AGC)[1], yet extensive areas are affected by disturbances, such as deforestation from agricultural expansion[2,3] and degradation from fires[4], selective logging[5], and edge effects[6,7]. Over time, disturbed forests can recover, gradually restoring carbon stocks and ecological functions[8]. However, how recovery rates vary with disturbance size, type and location remains poorly quantified. Here we use a bookkeeping approach with spatially explicit vegetation recovery curves to quantify AGC dynamics in disturbed tropical forests during 1990–2020. We find that disturbed tropical dry forests remained carbon neutral, whereas disturbed tropical humid forests experienced a net AGC loss of 15.6 ± 3.7 PgC, primarily driven by small but persistent deforestation clearings. Despite affecting only about 5% of the disturbed area, these small-size (less than 2 ha) deforestation events accounted for about 56% of carbon losses, owing to persistent land-use conversion without forest regrowth. By contrast, large fire-induced carbon losses were offset by the long-term post-fire recovery. Over time, deforestation expanded into humid forests with higher carbon stock density, intensifying AGC losses per unit area. These findings highlight the disproportionate impact of small clearings on tropical carbon losses, suggesting the need to curb land-use changes and protect young and recovering forests.

Tropical forests are essential to the global carbon (C) cycle, storing about 50% of the global forest aboveground carbon (AGC)[1]. However, a large portion of these forests experience disturbances such as deforestation caused by agricultural expansion[2,3] and degradation caused by fire[4], selective logging[5], and edge effects[6,7]. Over the past 30 years, 46% of tropical humid and dry forests have experienced some form of disturbance at least once, according to Landsat observations[9,10]. Although some forests are cleared and converted to non-forest land, most disturbed forests retain some tree cover but have reduced biomass and biodiversity, leading to degraded ecosystem functionality[11,12]. Over time, these disturbed forests can recover, gradually restoring the C stocks and ecological functions[8]. However, we have a limited understanding of how these rates vary with the size, type and location of disturbance. Quantification of forest C loss and subsequent post-disturbance biomass recovery is thus essential for understanding forests' substantial yet uncertain impact on the global C budget[13,14].

Young recovering forests accumulate C much faster than old-growth forests, but their sequestration potential varies across different climate conditions, forest types and disturbance agents[15–19]. Similarly, the type, magnitude and size of disturbance events impact C losses and subsequent C recovery[8,11,20,21]. For example, recovery after severe fires is slower than recovery following low-intensity windstorms[22]. Small-size disturbances create canopy gaps and increase edge exposure, which can amplify subsequent carbon losses through microclimatic stress and repeated degradation[23]. Previous studies have estimated forest recovery rates using site-based methods[15,24] and satellite-based approaches[25–27]. However, none has mapped the detailed spatial variations of both carbon losses and gains at a fine resolution across entire tropical forests owing to the limited availability of field data.

Here we present a bookkeeping model to estimate forest C losses and gains in disturbed tropical forests from 1990 to 2020 by integrating (sub)hectare-spatial-scale Earth observation data[9,10,28] on

[1]Laboratoire des Sciences du Climat et de l'Environnement, LSCE/IPSL, CEA-CNRS-UVSQ, Université Paris-Saclay, Gif-sur-Yvette, France. [2]Gamma Remote Sensing, Gümligen, Switzerland. [3]European Commission, Joint Research Centre (JRC), Ispra, Italy. [4]Department of Geosciences and Natural Resource Management, University of Copenhagen, Copenhagen, Denmark. [5]Ningbo Institute of Digital Twin, Eastern Institute of Technology, Ningbo, China. [6]Aerospace Information Research Institute, Chinese Academy of Sciences, Beijing, China. [7]GFZ Helmholtz Centre for Geosciences, Potsdam, Germany. [8]School of Geographical Sciences, University of Bristol, Bristol, UK. [9]CIFOR-ICRAF, Nairobi, Kenya. [10]The Nature Conservancy, Natural Climate Solutions Team, Arlington, VA, USA. [11]Centre de Recherche sur la Biodiversité et l'Environnement (CRBE), Université de Toulouse, IRD, Toulouse INP, Toulouse, France. [12]National Institute for Space Research (INPE), São José Dos Campos, Brazil. [13]Faculty of Environment, Science and and Economy, University of Exeter, Exeter, UK. [14]Department of Earth System Science, Ministry of Education Key Laboratory for Earth System Modeling, Institute for Global Change Studies, Department of Earth System Science, Tsinghua University, Beijing, China. [15]Département d'Informatique, École Normale Supérieure – PSL, Paris, France. [16]ISPA, UMR 1391, INRAE Nouvelle-Aquitaine, Bordeaux Sciences Agro (BSA), Université de Bordeaux, Bordeaux Villenave d'Ornon, France. ✉e-mail: philippe.ciais@lsce.ipsl.fr; wli2019@tsinghua.edu.cn

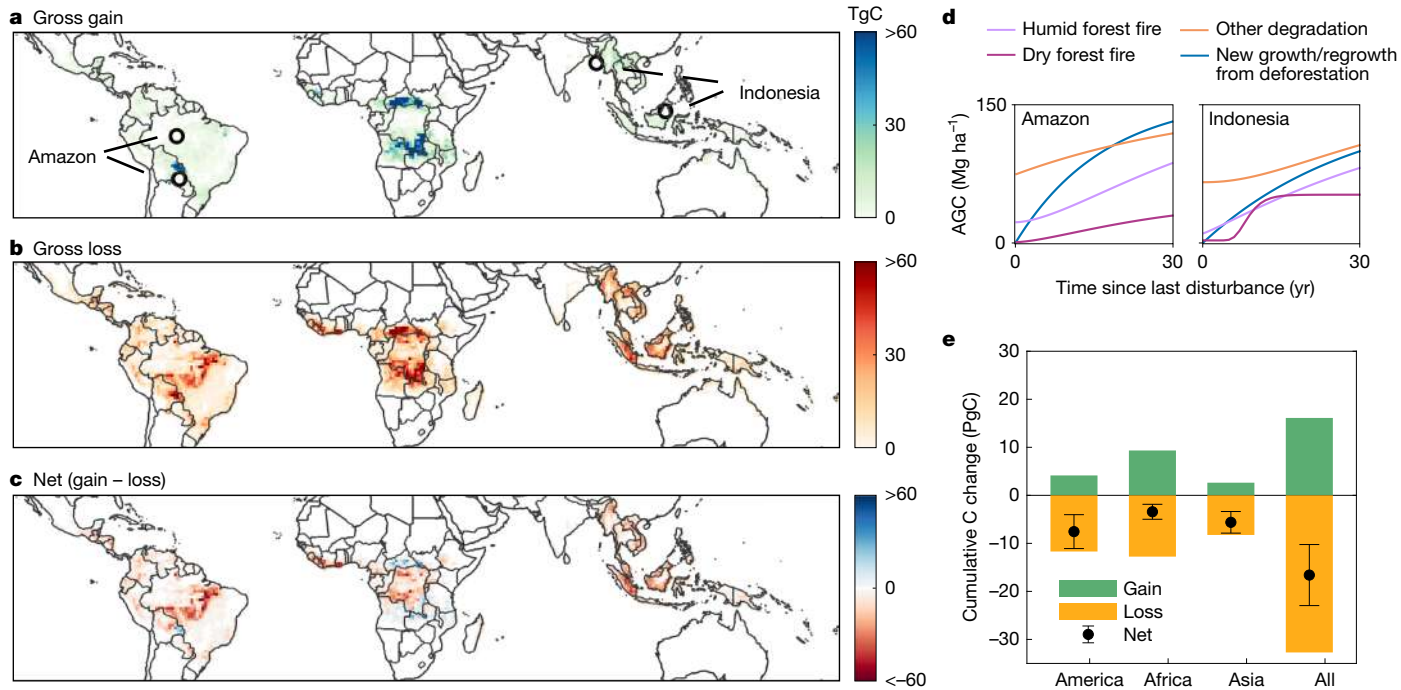

Fig. 1 | Cumulative AGC changes for tropical forests disturbed during 1990–2020. a–**c**, Spatial distribution of cumulative gross C gains (**a**), cumulative gross C losses (**b**) and cumulative net C changes (**c**). The net C changes, gross losses and gains are shown in units of TgC per 1° grid cell. **d**, Examples of the recovery curves in four 1° grid cells corresponding to the dry and humid forests (dashed and solid line in **a**, respectively) in the Amazon (left) and Indonesia (right). Curves from dry and humid forest sites are displayed within the same box for each region. **e**, Cumulative AGC changes for tropical Africa, America and Asia. Black dots represent the net C changes (sum of all gains and losses) for each tropical region, and the error bars indicate the corresponding standard errors. The recovery curves are given for forests affected by fire-driven degradation (humid or dry forests), other degradation, and regrowth from deforestation or new forest established in previously non-forested land. Administrative boundaries in **a**–**c** adapted from data © European Union, 1995–2025.

past disturbances with spatially explicit biomass recovery curves (Methods). Disturbed forests are defined here as forests experiencing deforestation and degradation since 1990, recovering from fire and non-fire degradation, or regrowing from deforestation and afforestation of non-forested areas (Methods and Extended Data Table 1). We constructed recovery curves specific to each type of disturbance in each forest region of the tropics, defined by 1° by 1° grid cells. To do so, we used a space-for-time approach, pairing present-day (2020) biomass with the time since the last disturbance at a fine resolution (30 m) across all past disturbances recorded in each 1° grid cell (Extended Data Fig. 1). This data-driven bookkeeping model detects the location of each disturbance each year, calculates C loss and then estimates recovery gain in subsequent years. In this way, we obtain a spatially explicit view of the AGC budget and its uncertainty (including deadwood; Methods) in tropical disturbed forests and identify the contributions of disturbances at different spatial scales.

Disturbed forests as a net AGC source

By combining spatially explicit biomass recovery curves that distinguish between recovery from fire and non-fire forest degradation, regrowth following deforestation, and new growth established from afforestation in non-forested land in each 1° grid cell (example grids are shown in Fig. 1e; flowchart in Extended Data Fig. 1), we tracked biomass losses and gains since 1990. Multiple sources of uncertainties were considered, including uncertainties from recovery curves, the biomass and the disturbance dataset (Supplementary Text 4). We found a net AGC loss of 16.6 ± 6.4 PgC, comprising a gross C loss of 32.7 ± 5.3 PgC from disturbances and a gross gain of 16.1 ± 4.3 PgC from recovery during 1990–2020. The hotspots of net C loss are located in the 'arc of deforestation' (the eastern and southeastern edges of the Amazon Basin), the Central Congo Basin, western Africa, Sumatra and the coastal regions of Borneo (Fig. 1b). Besides these previously reported hotspots[29,30], we also detected substantial but often understudied net AGC losses in South and Southeast Asian countries (Myanmar, Vietnam, Laos, Thailand and India). These countries together contributed net cumulative AGC losses of 1.6 ± 0.3 PgC, comparable in magnitude to Democratic Republic of the Congo (2.0 ± 1.7 PgC) and Indonesia (2.0 ± 0.6 PgC). Although a relatively small area was found to have experienced net C gains, we identified C-gain hotspots in African countries, such as the Central African Republic and Zambia. By multiplying the extent of the undisturbed forest and the net AGC accumulation rate from sites[31,32], we complemented the C budget of disturbed forests to obtain a pantropical C budget and estimated that the undisturbed forests were a net C sink, unlike disturbed forests. These undisturbed forests contributed to an AGC gain of 14.6 ± 4.4 PgC (Methods, Extended Data Fig. 2 and Supplementary Fig. 2), making the AGC balance of tropical forests close to neutral (cumulative loss of 2.0 ± 6.4 PgC, yearly net AGC loss of 0.07 ± 0.22 PgC yr^{-1}).

Transition of AGC-loss hotspots

Using annual maps of disturbances (Methods) as input into our bookkeeping model, we found that net AGC losses from tropical humid forests have increased since 1990 with two peak loss periods. The first loss peak, at a rate of 1.1 PgC yr^{-1}, was recorded between 1998 and 2001 (period 1). After this peak, net AGC losses declined, but a second, smaller peak of 0.5 PgC yr^{-1} was observed from 2013 to 2016 (period 2; Fig. 2a and Extended Data Fig. 3). The reduction in net AGC losses between the two peak periods was primarily owing to tropical America, particularly in Brazil, Bolivia and Colombia. The geographic epicentre of AGC losses shifted from humid forests in tropical America, which accounted for 47% of total AGC losses in period 1, to humid forests in tropical Africa, which contributed 38% in period 2 (Fig. 2a). After 2017,

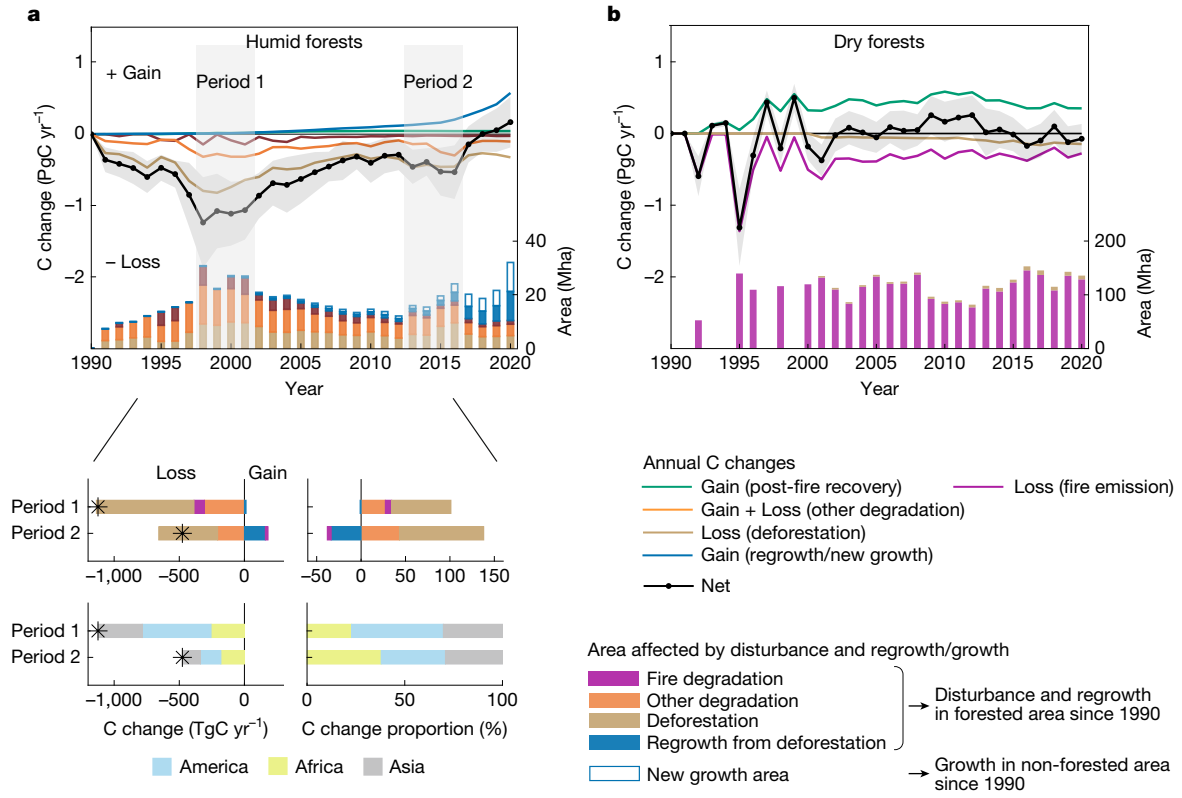

Fig. 2 | Temporal dynamics of forest C changes after disturbances in tropical forests during 1990–2020. a,**b**, Forest AGC gain and loss after fire-driven degradation, other degradation, deforestation, and regrowth from deforestation/new growth from tropical humid (**a**) and dry (**b**) forests. Two peaks with the largest forest C losses are shown in humid forests: 1998–2001 (period 1) and 2013–2016 (period 2). The black dots and shaded areas represent the annual net AGC balance by summing up all the C flux components and the corresponding standard errors. Black asterisks (bottom left) denote the net AGC balance for each period. Fire losses encompass both the instantaneous fire emission at the burning period and the legacy emission resulting from the decomposition of coarse woody debris. For visualization purposes, these losses are combined in this figure. Forest biomass loss and recovery after other degradation are also combined owing to the relatively small amount of AGC gain following other degradation. The bars represent the annual disturbed area associated with different disturbance types. Owing to the limited availability of Landsat data, there is a 5-year lacuna of burned areas in 1990s. As forest recovery generally takes longer to observe than rapid forest clearing, the recent forest regrowth and new growth from TMF carry a larger degree of uncertainty than earlier periods. Detailed contributions for each tropical region are provided in Extended Data Fig. 3.

humid forests transitioned from a net C source to a small C sink. The rapid increase in regrowth gain since 2017 is almost equally attributed to newly established forests and forest regrowth from previous clearings (Supplementary Fig. 3). However, part of this increase in young (re)growing forests might be re-cleared and reclassified in subsequent years owing to the dynamic nature of tropical land use, as discussed in Supplementary Text 8 and Supplementary Figs. 28–30. Overall, we found contrasting patterns in C dynamics between dry and humid forests. Since 1990, humid forests have lost 15.6 ± 3.7 PgC, equivalent to 6% of the tropical forest AGC stocks in 2020[1]. Dry forests, however, maintained a close-to-neutral C balance throughout the study period, with larger fluctuations in the early 1990s probably owing to the less-dense observations available during that time[33].

Small disturbances with larger C losses

Taking advantage of the gridded recovery curves, we analysed the contributions of disturbances to C changes across different disturbance-area size classes, which were classified into five patch-size categories (Methods). The smallest disturbances (≤2 ha) accounted for only 15% of the total disturbed area over the past 30 years. However, they were widely distributed, representing the most frequent patch-size class in 72% of 1° grid cells across the tropics (Fig. 3a). These smallest disturbances mostly correspond to small-scale deforestation and non-fire degradation events, whereas larger disturbance patches were mainly associated with fire-driven degradation (Fig. 3b and Extended Data Fig. 4). Between 1990 and 2020, the smallest disturbance size class contributed 45% of the gross and 71% of the net AGC losses (gross loss − gross gain), respectively. The net C losses from the smallest disturbances are primarily owing to deforestation associated with land-use transitions, where forests were converted to small-scale cropland, pastureland, roads and settlements[34], leading to persistent forest loss without subsequent biomass recovery. Recovery following non-fire small-scale degradation disturbances was slow, probably owing to persistent anthropogenic pressure, edge effects and microclimatic stress, which can inhibit natural regeneration for decades[6,16]. Overall, these small deforestation and non-fire degradation events cover only 5% and 4% of the total disturbed area, but they contribute disproportionately to the net AGC loss of 16.6 PgC. Small clearings alone account for 56% (9.3 PgC) of losses, and non-fire degradation for 25% (4.1 PgC). By contrast, medium-sized disturbances (between 2 ha and 1,000 ha) were smaller net C sources. Very large disturbances (>1,000 ha) were small net C sinks when summing up their C gains and losses over the past 30 years (Fig. 3b).

The disproportionate C losses and gains among different patch-size classes were particularly evident in Africa (Extended Data Fig. 5b). Although representing only 8% of the total disturbed areas in Africa, the smallest disturbances accounted for 106% of net AGC losses (this value exceeding 100% because net AGC gains from some other larger disturbance size classes offset part of the total losses) in this region. By contrast, 96% of the disturbances larger than 2 ha in dry tropical Africa were caused by repeated fires. Despite covering a larger area, these dry

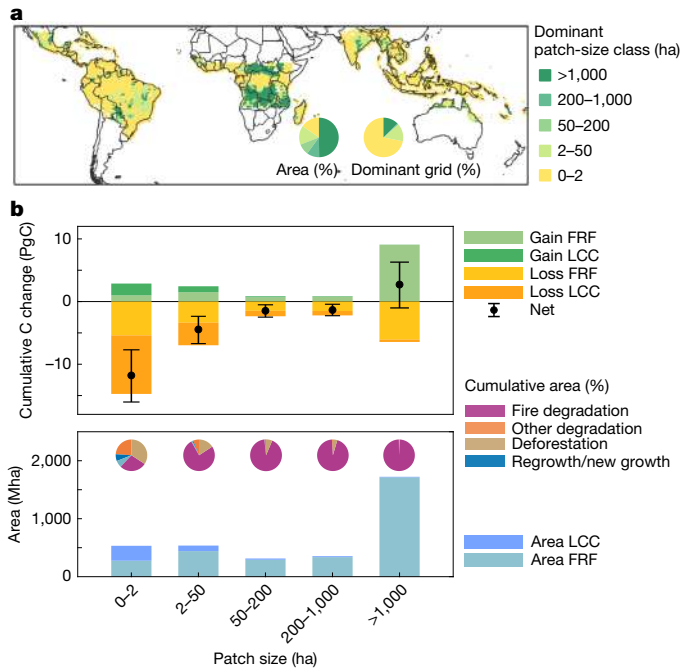

Fig. 3 | Net AGC balance changes for disturbed tropical forests associated with different disturbance patch sizes. a, Spatial distribution of the dominant disturbance patch class on the surface in each 1° grid cell. The two inset pie charts illustrate the area proportion of each patch-size class and the percentage of the dominant patch class across all 3,984 1° grid cells. **b**, Cumulative gross C gain, gross C loss, the net AGC changes and the associated area changes contributed by disturbances from different size classes over the past three decades. The black dots and error bars represent the net C balance and the corresponding standard errors for each disturbance patch-size class. The inset pie charts illustrate the cumulative percentage contribution of each disturbance type within each size class during 1990–2020. The C losses, gains and area changes are separated into FRF and LCC categories. FRF, disturbances occurring within the remaining forest, such as fire-driven degradation and other degradation. LCC, disturbances associated with forest land-cover change (permanent or temporary), such as deforestation or afforestation. Positive values indicate a C gain and negative values indicate a C loss. The C dynamics for each size class across tropical regions are shown in Extended Data Fig. 5. Administrative boundaries in **a** adapted from data © European Union, 1995–2025.

forests experienced only a small net AGC gain of 0.2 PgC (−6% of the net AGC losses) over the past 30 years, owing to post-fire vegetation recovery. This finding is consistent with independent coarse-scale L-band satellite measurements[30,35], in which dry tropical African forests were found to have net C-gain signals owing to post-fire recovery (Supplementary Text 5). In tropical South America and Southeast Asia, the smallest disturbances comprised a substantial portion of the disturbed area (41% and 49%) and also contributed notably to net AGC losses (56% and 72%; Extended Data Fig. 5a,c).

Shift towards humid C-dense forests

We found that disturbances from deforestation and non-fire degradation caused increasing gross AGC losses per unit area from 1990 to 2020 in humid forests (Fig. 4). This trend is explained by the encroachment of disturbances deeper into the interior of carbon-rich humid forests, as shown in South America and Southeast Asia[36,37]. In addition, deforestation creates edges where remaining forests meet open land. These edge forests degrade owing to changes in local climate and atmospheric mesoscale circulation[35], increased susceptibility to wind[38], higher fire risk under drier conditions[39] and greater exposure to human activities[11]. Consequently, disturbances often initiate at forest edges and progress inwards, leading to higher C loss per unit area.

By contrast, we observed a decreasing trend in gross AGC losses per unit area in dry forests, where losses are primarily attributed to fires (Fig. 4). Owing to increased temperatures, altered rainfall patterns and recurrent droughts, dry tropical forest fires have become more frequent and intense[40]. Repeated burning and more severe burning events tend to reduce AGC loss in subsequent fire events via a progressive exhaustion of fuel loads, eventually leading to a decline in AGC loss from burning events in dry tropical forests over time[16,41]. On the basis of the long-term burned-area maps used in this study[9], we found that 80% of the 30-m burned pixels in dry forests were repeatedly burned during 1990–2020, and 19% of the 1° grid cells showed an increasing trend of burning frequency during 1990–2020, particularly in the dry forests in Africa (Extended Data Fig. 6). Unlike humid forest fires in tropical Africa, which maintain a similar decreasing trend in AGC loss per unit area to those observed in dry forests, humid forest fires in tropical America show a contrasting trend, with fire activity increasingly encroaching into forests with higher AGC density (Extended Data Fig. 7). This trend may imply the expansion of slash-and-burn agriculture and the intensifying effects of extreme drought events, which reduce canopy moisture, increase flammability and facilitate fire spread into previously intact, high-carbon forests.

Discussion

A new window onto tropical AGC budget

By integrating (sub)hectare Earth observation data on past disturbances and biomass data to generate spatially explicit forest biomass recovery curves, our approach used 30-m-resolution activity data to estimate spatially explicit C losses and gains across all tropical forests in recent decades (30 years). Our model distinguishes how different disturbance drivers and sizes alter C dynamics. These factors are generally simplified or inadequately represented in dynamic global vegetation models and are also absent from nationally aggregated datasets and from the static, ad hoc average recovery curves used in bookkeeping models[42,43]. Global vegetation models are limited to human disturbances associated with land-use change, whereas our approach also maps losses and gains from natural disturbances, such as wildfires, blowdowns or droughts. A refined comparison of gross and net land-use change C fluxes would require a detailed classification of all disturbances into natural versus human-induced disturbances, which is a considerable challenge given the different definitions of anthropogenic disturbances across approaches[44].

Our estimates of total C losses and gains in disturbed tropical forests fall within a range comparable to those reported in previous satellite-based studies[13,26,45–48] (Supplementary Text 2.3 and Supplementary Table 5). However, our study provides unprecedented spatial and process detail for these numbers. Compared with the 'function of the mean' approaches that pooled data together by the tropical continent (hereafter 'continental-average curves', that is, in ref. 26), our spatially explicit recovery curves fitted at 1° grid resolution better capture local AGC dynamics (Supplementary Text 2.1 and Supplementary Fig. 10). The curves also reveal substantial geographic differences in recovery trajectories across the tropical forest biome (Fig. 1e and Supplementary Fig. 12a). Consequently, compared with our method based on spatially explicit curves, previous models based on continental-average curves have overestimated net AGC gains and losses in some regions, such as African dry forests (Supplementary Fig. 12d).

Limitations of the bookkeeping model

Despite providing unprecedented detail in the attribution of forest C dynamics through the integration of a global biomass dataset and Landsat-based disturbance records, our data-driven model is still constrained by the limitations of currently available yet imperfect remote-sensing products. Our model may underestimate minor disturbances (for example, small and low-intensity fires[38,49]) owing to the 30-m

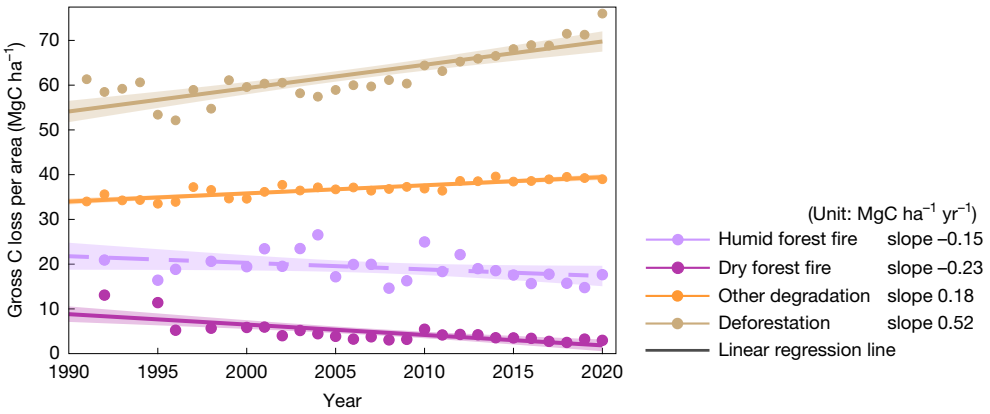

Fig. 4 | Temporal changes of gross forest AGC loss per unit of disturbed forest area caused by different types of disturbance from 1990 to 2020. The results for each tropical region are presented in Extended Data Fig. 7. The solid lines indicate statistically significant trends ($P < 0.01$) and the dashed lines represent non-significant trends. The shaded areas represent the 95% confidence intervals of the linear regression lines.

resolution of the Landsat data[10]. The crucial role of small disturbances in forest C loss could be better constrained by higher-resolution satellite imagery (for example, Planet and Sentinel)[50–52] and by attributing detailed disturbance agents (for example, selective logging and artisanal logging, shifting agriculture). However, such high-resolution data are only available for the past decade, thus lacking the temporal depth of Landsat. In general, the spatial and temporal patterns of burned areas derived from the global burned-area products[9] are consistent with the regional estimates from MapBiomas Fire[53] for Brazil (Supplementary Fig. 5). Similarly, the cumulative deforested area during 2000–2020 in this study, based on Tropical Moist Forest (TMF)[10], is also comparable to the records from Global Forest Watch (GFW)[28] in humid forests, despite some differences in temporal variations (Supplementary Fig. 7). These discrepancies probably arise from the distinct definitions of deforestation and tree cover loss, as well as different starting epochs (1990 and 2000, respectively) in the two datasets.

Our results are also impacted by uncertainties in the satellite-based biomass dataset (Climate Change Initiative, CCI Biomass) used to derive the recovery curves. For example, CCI Biomass may yield biased AGC estimates in regions where the model relating aboveground biomass to the satellite observations is poorly constrained, such as in Southeast Asia[54]. We tested whether the calculated C budget was sensitive to this effect using the CCI Biomass dataset archive, which improved the calibration of the retrieval algorithm over the five versions. Overall, the derived budgets indicate that tropical disturbed forests were a similar net carbon source during 1990–2020 (Supplementary Table 4 and Supplementary Text 3.2). The CCI Biomass map at the original 100-m resolution can blur C signals from fine-scale disturbances; nevertheless, it provides a valuable starting point for assessing the C impact of these understudied disturbances. Our study highlights the need for future global biomass products at finer resolutions to better capture the role of small-scale disturbances in forest carbon dynamics.

Our analysis excludes agricultural tree plantations (for example, rubber and industrial/smallholder oil palm plantations) in the humid tropics, which are inherent to the TMF dataset and methodology and have been filtered out owing to these tree crops. However, 'planted forests' (wood plantations that undergo periodic clear-cut harvesting and subsequent regrowth) may be included either as 'regrowing secondary forest' (post-harvest regrowth) or as afforestation in non-forested areas in both humid and dry forest domains. The potential impact of these planted forests on the disturbed area and the C changes (Supplementary Figs. 26 and 27 and Supplementary Table 6) is further explored in Supplementary Text 7. Another limitation is that our recovery curves did not explicitly consider changing environmental factors such as increasing atmospheric carbon dioxide, climate change, forest fragmentation[35], shifting species composition[55], and changes in the vulnerability and resilience of forests to extreme climate conditions[56]. Increasing high-resolution or long-term species maps and biomass datasets could help further explore these factors.

Protecting and restoring forests

Our study highlights that gross C losses from fire and non-fire degradation (−17.8 PgC) are even greater than deforestation losses (−14.9 PgC). In addition, post-degradation disturbance recovery gains remain insufficient to offset initial gross losses when averaged over the past 30 years. This underscores the need to curb deforestation and degradation in C loss hotspots and monitor regional transitions in hotspot areas from tropical America to Africa. By overlaying our spatially explicit C budget with the forest loss drivers map[2], we deduced that both large-scale commodity production and small-scale farming have driven C losses in South America. Conversely, 97% of the net C losses in Africa between 1990 and 2020 are attributed to small-scale agriculture (<2-ha disturbances). Additional pressure from village development and road construction further exacerbated the losses in Africa[57]. In response, sustainable agricultural practices, secure land tenure and support for agroforestry are essential to enhance the productivity of existing agricultural land, as well as to alleviate pressure on forest lands and avoid further C losses. In addition to avoiding human-induced disturbances in C-loss hotspots and C-rich forests, protecting young and recovering forests is crucial to effective carbon management, as repeated disturbances sharply reduce their carbon sequestration potential[16,19]. For example, we calculated that the forests disturbed before 2005 could have sequestered 3.1 PgC by 2050, yet 70% of these forests were cleared or re-disturbed between 2005 and 2020, halving their future carbon storage potential. We believe that implementing our data-driven model methodology, which uses spatially explicit recovery curves in global and national carbon assessments, provides valuable information for stakeholders to identify forest priority areas and optimize conservation efforts for mitigating carbon losses and enhancing forest recovery.

Online content

Any methods, additional references, Nature Portfolio reporting summaries, source data, extended data, supplementary information, acknowledgements, peer review information; details of author contributions and competing interests; and statements of data and code availability are available at https://doi.org/10.1038/s41586-025-09870-7.

1. Pan, Y. et al. The enduring world forest carbon sink. *Nature* **631**, 563–569 (2024).
2. Curtis, P. G., Slay, C. M., Harris, N. L., Tyukavina, A. & Hansen, M. C. Classifying drivers of global forest loss. *Science* **361**, 1108–1111 (2018).

3. Feng, Y. et al. Doubling of annual forest carbon loss over the tropics during the early twenty-first century. *Nat. Sustain.* **5**, 444–451 (2022).
4. Aragão, L. E. O. C. & Shimabukuro, Y. E. The incidence of fire in Amazonian forests with implications for REDD. *Science* **328**, 1275–1278 (2010).
5. Asner, G. P. et al. Selective logging in the Brazilian Amazon. *Science* **310**, 480–482 (2005).
6. Silva Junior, C. H. et al. Persistent collapse of biomass in Amazonian forest edges following deforestation leads to unaccounted carbon losses. *Sci. Adv.* **6**, eaaz8360 (2020).
7. Zhu, L. et al. Comparable biophysical and biogeochemical feedbacks on warming from tropical moist forest degradation. *Nat. Geosci.* **16**, 244–249 (2023).
8. Poorter, L. et al. Multidimensional tropical forest recovery. *Science* **374**, 1370–1376 (2021).
9. Long, T. et al. 30 m resolution global annual burned area mapping based on Landsat images and Google Earth Engine. *Remote Sens.* **11**, 489 (2019).
10. Vancutsem, C. et al. Long-term (1990–2019) monitoring of forest cover changes in the humid tropics. *Sci. Adv.* **7**, eabe1603 (2021).
11. Bourgoin, C. et al. Human degradation of tropical moist forests is greater than previously estimated. *Nature* **631**, 570–576 (2024).
12. Bullock, E. L., Woodcock, C. E., Souza, C. Jr. & Olofsson, P. Satellite-based estimates reveal widespread forest degradation in the Amazon. *Glob. Change Biol.* **26**, 2956–2969 (2020).
13. Baccini, A. et al. Tropical forests are a net carbon source based on aboveground measurements of gain and loss. *Science* **358**, 230–234 (2017).
14. Pugh, T. A. M. et al. Role of forest regrowth in global carbon sink dynamics. *Proc. Natl Acad. Sci. USA* **116**, 4382–4387 (2019).
15. Cook-Patton, S. C. et al. Mapping carbon accumulation potential from global natural forest regrowth. *Nature* **585**, 545–550 (2020).
16. Heinrich, V. H. A. et al. Large carbon sink potential of secondary forests in the Brazilian Amazon to mitigate climate change. *Nat. Commun.* **12**, 1785 (2021).
17. Moreno-Mateos, D. et al. Anthropogenic ecosystem disturbance and the recovery debt. *Nat. Commun.* **8**, 14163 (2017).
18. Gao, X. et al. The importance of distinguishing between natural and managed tree cover gains in the moist tropics. *Nat. Commun.* **16**, 6092 (2025).
19. Robinson, N. et al. Protect young secondary forests for optimum carbon removal. *Nat. Clim. Change* **15**, 793–800 (2025).
20. Lapola, D. M. et al. The drivers and impacts of Amazon forest degradation. *Science* **379**, eabp8622 (2023).
21. Muller-Landau, H. C. et al. Patterns and mechanisms of spatial variation in tropical forest productivity, woody residence time, and biomass. *New Phytol.* **229**, 3065–3087 (2021).
22. Chazdon, R. L. Tropical forest recovery: legacies of human impact and natural disturbances. *Perspect. Plant Ecol. Evol. Syst.* **6**, 51–71 (2003).
23. Cushman, K. C. et al. Impact of a tropical forest blowdown on aboveground carbon balance. *Sci. Rep.* **11**, 11279 (2021).
24. Poorter, L. et al. Biomass resilience of Neotropical secondary forests. *Nature* **530**, 211–214 (2016).
25. Chen, N. et al. Revealing the spatial variation in biomass uptake rates of Brazil's secondary forests. *ISPRS J. Photogramm. Remote Sens.* **208**, 233–244 (2024).
26. Heinrich, V. H. A. et al. The carbon sink of secondary and degraded humid tropical forests. *Nature* **615**, 436–442 (2023).
27. Holcomb, A., Mathis, S. V., Coomes, D. A. & Keshav, S. Computational tools for assessing forest recovery with GEDI shots and forest change maps. *Sci. Remote Sens.* **8**, 100106 (2023).
28. Hansen, M. C. et al. High-resolution global maps of 21st-century forest cover change. *Science* **342**, 850–853 (2013).
29. Csillik, O. et al. A large net carbon loss attributed to anthropogenic and natural disturbances in the Amazon arc of deforestation. *Proc. Natl Acad. Sci. USA* **121**, e2310157121 (2024).
30. Feng, Y. et al. Global patterns and drivers of tropical aboveground carbon changes. *Nat. Clim. Change* **14**, 1064–1070 (2024).
31. Hubau, W. et al. Asynchronous carbon sink saturation in African and Amazonian tropical forests. *Nature* **579**, 80–87 (2020).
32. Qie, L. et al. Long-term carbon sink in Borneo's forests halted by drought and vulnerable to edge effects. *Nat. Commun.* **8**, 1966 (2017).
33. Wulder, M. A. et al. The global Landsat archive: status, consolidation, and direction. *Remote Sens. Environ.* **185**, 271–283 (2016).
34. Masolele, R. N. et al. Mapping the diversity of land uses following deforestation across Africa. *Sci. Rep.* **14**, 1681 (2024).
35. Zhao, Z. et al. Central African biomass carbon losses and gains during 2010–2019. *One Earth* **7**, 506–519 (2024).
36. Song, X.-P., Huang, C., Saatchi, S. S., Hansen, M. C. & Townshend, J. R. Annual carbon emissions from deforestation in the Amazon Basin between 2000 and 2010. *PLoS ONE* **10**, e0126754 (2015).
37. Xu, Y. et al. Recent expansion of oil palm plantations into carbon-rich forests. *Nat. Sustain.* **5**, 574–577 (2022).
38. Espírito-Santo, F. D. B. et al. Size and frequency of natural forest disturbances and the Amazon forest carbon balance. *Nat. Commun.* **5**, 3434 (2014).
39. Cochrane, M. A. & Laurance, W. F. Synergisms among fire, land use, and climate change in the Amazon. *AMBIO* **37**, 522–527 (2008).
40. Silvestrini, R. A. et al. Simulating fire regimes in the Amazon in response to climate change and deforestation. *Ecol. Appl.* **21**, 1573–1590 (2011).
41. Saito, M. et al. Fire regimes and variability in aboveground woody biomass in miombo woodland. *J. Geophys. Rese. Biogeosci.* **119**, 1014–1029 (2014).
42. Hansis, E., Davis, S. J. & Pongratz, J. Relevance of methodological choices for accounting of land use change carbon fluxes. *Glob. Biogeochem. Cycles* **29**, 1230–1246 (2015).
43. Houghton, R. & Nassikas, A. A. Global and regional fluxes of carbon from land use and land cover change 1850–2015. *Glob. Biogeochem. Cycles* **31**, 456–472 (2017).
44. Grassi, G. et al. Reconciling global-model estimates and country reporting of anthropogenic forest CO_2 sinks. *Nat. Clim. Change* **8**, 914–920 (2018).
45. Achard, F. et al. Determination of tropical deforestation rates and related carbon losses from 1990 to 2010. *Glob. Change Biol.* **20**, 2540–2554 (2014).
46. Harris, N. L. et al. Global maps of twenty-first century forest carbon fluxes. *Nat. Clim. Change* **11**, 234–240 (2021).
47. Pearson, T. R. H., Brown, S., Murray, L. & Sidman, G. Greenhouse gas emissions from tropical forest degradation: an underestimated source. *Carbon Balance Manag.* **12**, 3 (2017).
48. Xu, L. et al. Changes in global terrestrial live biomass over the 21st century. *Sci. Adv.* **7**, eabe9829 (2021).
49. Khairoun, A., Mouillot, F., Chen, W., Ciais, P. & Chuvieco, E. Coarse-resolution burned area datasets severely underestimate fire-related forest loss. *Sci. Total Environ.* **920**, 170599 (2024).
50. Dalagnol, R. et al. Mapping tropical forest degradation with deep learning and Planet NICFI data. *Remote Sens. Environ.* **298**, 113798 (2023).
51. Dupuis, C., Fayolle, A., Bastin, J.-F., Latte, N. & Lejeune, P. Monitoring selective logging intensities in central Africa with Sentinel-1: a canopy disturbance experiment. *Remote Sens. Environ.* **298**, 113828 (2023).
52. Slagter, B. et al. Monitoring direct drivers of small-scale tropical forest disturbance in near real-time with Sentinel-1 and -2 data. *Remote Sens. Environ.* **295**, 113655 (2023).
53. Alencar, A. A. C. et al. Long-term Landsat-based monthly burned area dataset for the Brazilian biomes using deep learning. *Remote Sens.* **14**, 2510 (2022).
54. Santoro, M. et al. Design and performance of the Climate Change Initiative Biomass global retrieval algorithm. *Sci. Remote Sens.* **10**, 100169 (2024).
55. Enright, N. J., Fontaine, J. B., Bowman, D. M., Bradstock, R. A. & Williams, R. J. Interval squeeze: altered fire regimes and demographic responses interact to threaten woody species persistence as climate changes. *Front. Ecol. Environ.* **13**, 265–272 (2015).
56. Bennett, A. C. et al. Sensitivity of South American tropical forests to an extreme climate anomaly. *Nat. Clim. Change* **13**, 967–974 (2023).
57. Shapiro, A. et al. Small scale agriculture continues to drive deforestation and degradation in fragmented forests in the Congo Basin (2015–2020). *Land Use Policy* **134**, 106922 (2023).

Methods

Humid and dry forest extent

Our study area covers the same study domain as the TMF datasets[10], which approximately overlaps the 'tropical rainforest', 'tropical moist forest', 'tropical mountain system' and 'tropical dry forest' zones from the Food and Agriculture Organization global ecological zones. We used pixels belonging to the classes of forest cover and changes from the TMF transition map (summarizing 31 years of forest dynamics) to define the humid forest extent. For the dry forest, we delineated the extent by removing the humid forest extent from a global tree cover map[28] for the year 2000 with a tree cover threshold of >25%, following ref. 58. The total tropical forest extent is 1,898 Mha, which aligns closely with the estimates from the forest inventory (1,872 Mha)[1]. Humid forests account for 65% of the total forest area, whereas tropical dry forests cover 667 Mha (35%) (Supplementary Fig. 1).

Forest disturbances attribution

We used annual forest change maps from TMF (version 2023) datasets[10], global annual burned area maps (GABAM)[9], and the global tree cover loss and gain maps from GFW[28] to track forest disturbance history from 1990 to 2020 in humid and dry forests in the tropics, respectively. We chose GABAM as the fire product owing to its long period (starting from 1985) and its comprehensive coverage of tropical forests. Although the global burned-area products used in this study[9] may underestimate fire in certain regions[59,60], their spatial and temporal patterns are generally consistent with the annual burned-area estimates from a regional dataset[53] for Brazil (Supplementary Fig. 5) and a global dataset[61] for the tropics (Supplementary Fig. 6). Owing to the lack of continuous forest cover change products in dry forests before 2000, we may also underestimate the forest loss in dry forests before 2000. All the above products were derived based on a pixel-level classification of Landsat satellite images and have been validated using independent ground samples (Supplementary Text 1).

For humid forests, we identified four types of disturbance and recovery processes: fire-driven degradation, other degradation, deforestation, and forest regrowth from deforested areas or non-forest areas. The first two types, which occur within existing forest areas, are grouped under the 'forest land remaining forest land' category. The latter two, associated with permanent or temporary land-cover change (LCC), are classified under the 'LCC' category. These disturbance types categorize regions into fire-degraded forests, other degraded forests, deforested areas and regrowth forests (Extended Data Table 1).

Deforested areas and regrowth forests in humid forests were derived from annual change maps from TMF datasets. Following the TMF definition, deforestation refers to the long-term conversion (disturbance of more than 2.5 years duration or an occurrence of more than four short-duration disturbance events) of land from forest to non-forest areas[10]. By contrast, forest degradation includes natural events (for example, hurricanes, droughts or blowdowns), as well as selective logging or fire that does not involve a land-use change. Still, it is characterized by a temporary decline in canopy cover and biomass owing to short-term disturbances (shorter than 2.5 years) followed by recovery[11]. Fire-degraded forests in humid forests were identified by overlapping the extent of humid forests (including undisturbed and disturbed forests) with the fire history[9], which does not distinguish between forest and non-forest fires. Deforested areas where fire and deforestation co-occurred were removed from fire-degraded forests to ensure that only forest fires followed by forest recovery were included in the fire degradation category. The other non-fire-degraded forests were derived using the pixels classified as degradation from the TMF's annual change maps, excluding pixels identified as fire-degraded forests. The fire-deforested area was not explicitly separated because it does not encompass the post-fire recovery process. However, the area affected by fire-driven deforestation and its associated C changes is presented separately in Supplementary Table 1. Regrowth forests were further categorized into two groups: newly established forests from non-forested areas, dating back to the beginning of TMF in 1990, and regenerating forests following deforestation, based on existing forest extent and 31-year deforestation records.

As detailed disturbance datasets are unavailable for tropical dry forests, we attributed forest fires by overlapping the dry forest extent with burned history[9]. A canopy height map[62] with a threshold of 5 m was applied to determine whether the burned forests are recovering (hereafter referred to as fire-degraded forests) in the dry domain. Deforestation in dry forests was determined separately using tree-cover-loss maps from the GFW. Similarly, pixels with tree cover gain[28] and a canopy height larger than 5 m were removed in areas classified as deforested. Other causes of forest degradation and recovery from non-fire are not thoroughly analysed in the dry domain.

Forest biomass regrowth after disturbance

Owing to the lack of biomass data with temporal and spatial granularity comparable to the Landsat dataset, a space-for-time approach was used to construct forest biomass recovery curves for each 1° grid cell by combining the disturbance history and the 2020 aboveground biomass dataset at 100-m resolution from v4 CCI Biomass[63]. The original aboveground biomass map was converted to aboveground biomass carbon (AGC) using a scaling factor of 0.5 (ref. 64). We first calculated the time since the last disturbance based on the combined disturbance maps (GABAM, TMF and tree-cover-loss maps from GFW) for all types of disturbance, as described in the above section. We then derived the AGC values for each annual age class (that is, each year since the last disturbance) by overlapping the AGC map with the time since last disturbance map. The AGC map was resampled to 30 m using the nearest interpolation to match the pixel spacing of the disturbance datasets. To mitigate the impact of the coarser resolution, we fitted the recovery curves using disturbances with areas larger than 1 ha and more than 10 connected 30-m pixels. Besides, we randomly selected 100 1° grid cells and tested the bilinear resampling algorithm to downscale the AGC maps. The choice of the resampling algorithm did not substantially change the derived recovery curves and C changes. At the 1° grid cell, an average of 20%, 2% and 21% of the 30-m pixels experienced forest regrowth, fire-driven degradation and other degradation, respectively. This number of pixels was sufficient to provide a detailed disturbance history, enabling the definition of a recovery curve. The average number of times since the last disturbances was 24 and 8 at the 1° grid for building the recovery curves in humid and dry forests, respectively. Still, 13% of the grid cells failed to fit the recovery curves for each type of disturbance because they did not have multiple disturbances (>3). We, therefore, used the curves from the nearest grid cell in the following C accounting models.

A Chapman–Richards growth function ('Growth', equation (1)) was applied to delineate the relation between the AGC from the satellite-based AGC maps and the time since the last disturbance at each 1° grid cell.

$$\mathrm{Growth}_{ti} = \mathrm{AGC}_{\max} \times (1 - e^{(-b \times ti)})^{c} + d \quad (1)$$

$\mathrm{AGC}_{\max}$ denotes asymptotic AGC, which determines the maximum potential AGC the forest could reach, t and i refer to the time since the last disturbance in the humid forests and the fire return interval in the dry forests, respectively. The parameters b, c and d denote the recovery curves' rate, shape and intercept, respectively.

The recovery curves were derived for each grid cell in humid forests, considering three types of disturbance: fire-driven degradation, other degradation and forest regrowth. For fire and non-fire-degraded forests where only partial AGC is removed, d represents the remaining AGC after degradation. In the case of forests regrowing from non-forested or deforested land, d equals 0.

To reflect the long-term recovery potential of forests, we assumed that forest AGC eventually returns to levels typical of old-growth stands, following the approach of ref. 26. Accordingly, the 85th percentile of the forest AGC in each grid cell was used to determine AGC_{max} for humid forests. The 85th percentile was selected to minimize the differences (mean differences of 1.2 MgC ha^{-1}) at the gridded level between the AGC density of the intact forest by overlapping the 2020 intact forest layer[65] and the gridded AGC maps (Supplementary Fig. 24). Additional sensitivity tests using the curves based on the 75th and 95th percentiles of the forest AGC produced similar gross C gains, indicating that the choice of different percentiles has a limited impact on the overall budget (Supplementary Table 4).

Unlike humid forests, dry forests are prone to fire with more recurrent burns and shorter fire return intervals (Supplementary Fig. 4). In this biome, studies have shown a shift in fire regimes and a potential change in forest recovery and resilience[66,67]. In some cases, the forests could recover to the initial pre-fire equilibrium if the fire return period is longer than the recovery time needed for the forests. In other cases, recovery is vulnerable to reduced fire return intervals[55], and the equilibrium could be reset. Therefore, AGC_{max} was taken as an unknown variable and determined by model fitting. Thirty-five per cent of the derived AGC_{max} are lower than the average AGC from the intact forest layer in the dry domain[65]. Similarly, we constructed recovery curves in dry forests using AGC and the mean fire return interval, rather than the time since the last disturbance. The mean fire return interval was calculated by dividing the length of the study period (1990–2020) by the number of fires detected for each 30-m pixel during the same period, following ref. 68.

To compare the gridded recovery curves with the approach based on the continental-average curves, we also fitted the recovery curves using the median AGC across the three tropical regions at each age/fire return interval class for each type of disturbance based on the same biomass and disturbance datasets, following a similar approach from ref. 26. Overall, the gridded recovery curves showed better agreement with field and satellite observations and captured greater regional variability in recovery rates across the tropics than the continental-average curves. Although the two approaches yielded similar total C budgets, they differed substantially in the spatial distribution of C fluxes. Further details are provided in Supplementary Text 2.1.

We also tested different grid sizes and growth functions (Supplementary Text 3.1). A grid size of 1° × 1° was selected, as the model fitting performance improved with increasing grid size from 0.25° to 1° (Supplementary Table 3). Alternative growth functions produced similar AGC accumulation patterns (Supplementary Fig. 22). We therefore adopted the Chapman–Richards function for its flexibility in representing diverse recovery trajectories, including both sigmoidal and exponential shapes.

Spatially explicit AGC counting model

Disturbed forest. Using a spatially explicit bookkeeping model, we estimated the AGC changes in the disturbed forests in the tropics during 1990–2020. In time and space, we then tracked all the 30-m biomass losses and gains consecutive to each disturbance event (mentioned above) with a data-driven C accounting model[69] from 1990 to 2020. The forest loss term consisted of the AGC losses from (1) the forest remains forest (FRF) category, which included degradation fires (L_{fire}) and other degradation (L_{deg}), and (2) the losses from forests associated with LCC category (that is, forest to non-forest, deforestation (L_{def})). The gain term included the forest biomass recovery after fire (G_{fire}), other degradation (G_{deg}) from the FRF category and regrowth (G_{reg}) from the LCC category (equation (2)). It is noted here that the losses from degradation fires are not associated with deforestation. Losses by other non-fire degradation are calculated in L_{deg}. The area and C losses caused by fire/non-fire deforestation and degradation are shown in Supplementary Table 1. The regrowth gains (G_{reg}) are further separated into C gains from afforestation (newly established forests from non-forested areas since the beginning of the TMF in 1990) and reforestation (regrowing forests following deforestation) (equation (3) and Supplementary Fig. 3).

$$\text{AGC change} = G_{fire} - L_{fire} + G_{deg} - L_{deg} + G_{reg} - L_{def} \quad (2)$$

$$G_{reg} = G_{\text{regrow from deforestation}} + G_{\text{new growth}} \quad (3)$$

For each type of disturbance followed by forest recovery, the forest biomass gain depends on the recovery rate derived from the recovery curves at the corresponding grid cell and the period between two disturbance events. The recovery curves for different disturbance types (fire-driven degradation, other degradation and regrowth in humid forests) and fire degradation in dry forests were applied to the corresponding disturbance events. Here the AGC increase after each disturbance event is calculated using the recovery curves and the disturbed area as follows (equation (4)):

$$G = \sum_{t=1990}^{2020} \text{Area}_t \times \sum_{ti=0}^{p} (\text{Growth}_{ti+1} - \text{Growth}_{ti}) \quad (4)$$

where t denotes the year when the disturbance happens, Area_t denotes the disturbance area at year t, and p is the period between the two disturbances. If only one disturbance occurs during 1990–2020, p equals $2020 - t$.

Forest biomass loss owing to disturbance was related to the disturbance types and the pre-disturbance AGC density (equation (5)). The loss ratio for each disturbance event was determined using maximum AGC and the initial AGC (intercept) from the corresponding recovery curve (equation (6)). In dry and humid forests, all forest biomass was removed during deforestation events (ratio = 1), whereas partial AGC remained after fire and non-fire degradation (ratio < 1).

$$L_{deg/def} = \sum_{t=1990}^{2020} \text{Area}_t \times \text{AGC}_t \times \text{ratio} \quad (5)$$

$$\text{ratio} = (\text{AGC}_{max} - d)/\text{AGC}_{max} \quad (6)$$

where AGC_t denotes the pre-disturbance AGC density at the year of disturbance t.

For the first disturbance during the study period, AGC_t was determined by the AGC value from the nearest forest pixel, which was not disturbed during 1990–2020 but could be disturbed by the disturbances before 1990. AGC density for the nearest forest pixel, including disturbed and undisturbed forests, was used as the lower bound and the value from the maximum potential AGC (AGC_{max}) was used as the upper bound for the sensitivity test. All sensitivity tests consistently indicated that tropical disturbed forests acted as net C sources during 1990–2020 (Supplementary Table 4). For the subsequent disturbances, AGC_t was estimated from the previous disturbance and its following recovery trajectory. Using biomass data from the original dataset with the 100-m spatial resolution might have introduced uncertainty when calculating the C loss for disturbances smaller than 1 ha. To explore mixing effects from surrounding pixels, we applied AGC_t, derived from the nearest undisturbed forest patch larger than 1 ha (equal to one 100-m AGC pixel in the AGC dataset), to the disturbed forest pixel as its pre-disturbance AGC value. We applied a sensitivity test without the size threshold (including forest pixels smaller than 100 m). The derived C budget shows a similar disproportionate C loss among different disturbance size classes (Supplementary Fig. 8).

For each fire event, not all the biomass supposed to be burned is immediately emitted. Although fire causes an instantaneous release of C to the atmosphere at the year of burning (t), a portion of the unburned biomass is converted into coarse woody debris (CWD),

which decomposes gradually over time[70]. Therefore, we further separated the instant AGC loss and legacy emissions from the decomposition of CWD for fire-induced C losses (equation (7)). The instantaneous fire emission was calculated using the pre-fire AGC and a coefficient determining the fraction of immediate AGC release to the atmosphere by fire, that is, combustion completeness (cc). The legacy emission from CWD decay was calculated based on the amount of the newly fire-formed CWD converted from the remaining living AGC (equation (8)) and the decay of the CWD that follows a global exponential rule[71] (equation (9)).

$$L_{\text{fire}} = \sum_{t=1990}^{2020} \text{Area}_t \times \left[\text{AGC}_t \times \text{cc} + \sum_{ti=0}^{2020-t} (\text{CWD}_{ti+1} - \text{CWD}_{\text{ti}}) \times \text{cue} \right] \quad (7)$$

$$\text{CWD}_0 = (1 - \text{cc}) \times \text{AGC}_t \quad (8)$$

$$\text{CWD}_{ti} = \text{CWD}_0 \times e^{(-k \times ti)} \quad (9)$$

where CWD_{ti} denotes the remaining CWD after the years since the last fire, CWD_0 defines the newly formed CWD from the fire event at year t, k is a constant value that determines the annual decay rate of CWD through the decomposition process, cc represents the combustion completeness value, and cue denotes the microbial carbon use efficiency.

To determine the portion of the immediate AGC loss at burning time, we applied gridded forest cc at 500 m from a previous study[61]. k was derived from site-observed biotic woody decay rates spanning the tropics from a previous study[72]. As not all the AGC is directly emitted to the atmosphere through CWD decomposition, we applied a cue ratio, which partitions C transferring from litter into the soil in the calculation. A cue of 50% was adopted following the Century model[73].

Undisturbed forest. To understand AGC changes in all tropical forests, we further estimated AGC changes in undisturbed forests. This was done by multiplying the extent of remaining undisturbed forest areas for each study year by the average net AGC accumulation rate with ±1 s.d. derived from site observations in the three tropical continental regions[31,32]. We used forest pixels classified as undisturbed forest from TMF as the undisturbed forest extent for humid forests, and the forest pixels with AGC higher than the 85th percentile of all the dry forest pixels in each 1° grid as undisturbed forests in the dry domains.

Disturbance patch-size identification

We first segmented disturbance patches for the patch analysis by aggregating adjacent 30-m pixels disturbed in the same year and of the same disturbance type based on the combined disturbance datasets. The adjacent disturbed pixels were identified using the eight-neighbour rule by checking all eight surrounding cells (north, south, east, west and diagonals). We then calculated the size of each disturbance patch over the past 30 years and categorized them into five size groups: 0–2 ha, 2–50 ha, 50–200 ha, 200–1,000 ha and >1,000 ha. Disturbances smaller than 2 ha were classified as the smallest disturbances, typically associated with selective logging activity, natural events or, to a lesser extent, smallholder activity. We further analysed patch sizes for each disturbance type and the corresponding biomass gain and loss within each size category. We also adjusted the minimum area threshold for the smallest size class from 1 ha to 10 ha and found the smallest class consistently contributed to the largest C losses (Supplementary Fig. 9).

Drivers of disturbances

To attribute forest disturbances and the induced C changes to their drivers, we utilized the tree-cover-loss-driver map from ref. 2, which determined the dominant drivers of tree cover loss into five categories: commodity-driven deforestation, shifting agriculture, forestry, wildfires and urbanization. Given that commodity-driven deforestation is owing to the expansion of large-scale agricultural plantations and shifting agriculture is usually small and patchy farming systems, we reclassified commodity-driven deforestation as commodity-driven agriculture and shifting agriculture as small-scale agriculture following ref. 3. The driver map at a coarse 10-km resolution may introduce uncertainty in attributing the drivers. As a supplement, we further explored the potential impact of shifting agriculture and selective logging at 30 m using the TMF and ancillary datasets (details in Supplementary Text 6 and Supplementary Fig. 25).

Evaluation of the recovery and AGC models

The recovery curves were validated using field-based observations[15,24]. A total of 348 sites with 1,447 observations at different ages were collected, with 60, 1,157 and 230 measurements in tropical Africa, America and Asia. We compared the field-based AGC and the AGC derived from the spatially explicit regrowth curves following deforestation at the same grid in the corresponding age intervals (Supplementary Text 2.1, Supplementary Fig. 10 and Supplementary Table 2). Similarly, the continental-average curves are binned at the corresponding age interval and compared with the field-based AGC. The comparison shows that the spatially explicit curves closely matched the site measurements across the three tropical continents, being in better agreement than those obtained from the continental-average curves (Supplementary Fig. 10). In addition, we compared the AGC gain rate for the regrowth forests at young stages (age <20) with the previous studies based on remote sensing and site observations. Our estimated AGC gain rate for the regrowth forests was higher than the previous satellite-based studies in tropical America and Asia and matched well with the mean values reported by field sites and inventories (Supplementary Fig. 11). Despite this overall consistency, 16% of grid cells showed extremely rapid increases at early stages when compared with the AGC gain rate map from ref. 15. These anomalies may arise from the temporal lag between the actual onset of forest regrowth and the satellite-based detection, as well as the overestimation of biomass data in some regions. We thus conducted a sensitivity analysis using a Bayesian calibration approach to adjust these anomalies and explored the impact on overall C changes (Supplementary Text 3.1 and Supplementary Figs. 20 and 21). As fast regrowth following deforestation accounts for only 3% of the total disturbed forests, whereas deforestation with no forest regrowth and the slow recovery following degradation dominated the outsized impact from small-scale disturbances, this correction has a limited impact on the overall C budget (Supplementary Text 3.1).

We further compared our modelled AGC with the satellite-based AGC in 2019[63] (Supplementary Figs. 13 and 14). This sanity check is important because if our spatially explicit bookkeeping model accurately captures AGC changes after disturbances, the AGC in disturbed pixels in 2019 should fall within the range of satellite AGC maps. It is partly independent because the recovery curves represent the average regrowth trajectory at the grid level and the biomass losses and gains vary at each 30-m pixel for each disturbance event (for example, low-severity degradation). The 2019 biomass dataset was not used to develop the growth curves, whereas the 2020 biomass map was. Each annual CCI Biomass map is derived from year-specific, independent synthetic aperture radar (SAR) observations[54], which minimizes circularity between years. The model performance based on the models with spatially explicit recovery curves was also compared with those based on continental-average curves (Supplementary Text 2.1 and Supplementary Figs. 12 and 15). For each disturbed forest pixel, the forest AGC density for the year 2019 (AGC_{2019}) is expressed as follows (equation (10))

$$\text{AGC}_{2019} = \sum_{t=1990}^{2019} \left(\sum_{ti=0}^{p} [\text{Growth}_{ti+1} - \text{Growth}_{ti}] - \Delta\text{AGC}(t) \right) \quad (10)$$

where $\Delta AGC(t)$ denotes the loss of living AGC due to the disturbance in year t, and p is the period between the two disturbance events.

AGC density changes induced by the disturbances from 1990 to 2019 were added to calculate the AGC density in 2019.

Third, we also validated the modelled AGC with independent lidar-based biomass measurements[74,75] at different years. We found that the C accounting model integrated with recovery curves can generally reproduce AGC regrowth following disturbances across different tropical continents, regardless of disturbance type (Supplementary Text 2.2 and Supplementary Figs. 16–19).

Uncertainties for the AGC counting model

We considered multiple sources of uncertainty in our bookkeeping model (Supplementary Fig. 23), including parametric uncertainty from the growth curves, observational uncertainty from the CCI Biomass dataset and classification uncertainty in the disturbance dataset. We combined the uncertainties from each AGC change component and the annual changes using the root sum of squares method to calculate the overall net AGC uncertainty. The details are described in Supplementary Text 4.

Data availability

The ESA-CCI Biomass dataset is available at https://climate.esa.int/en/odp/#/project/biomass. The burned-area dataset can be accessed from https://vapd.gitlab.io/post/gabam/. The TMF data are available at https://forobs.jrc.ec.europa.eu/TMF. The tree cover loss from GFW can be accessed from https://www.globalforestwatch.org/. The spatially explicit recovery curves derived in this study are available on Zenodo via https://zenodo.org/records/15869647 (ref. 76). Source data are provided with this paper.

Code availability

The scripts used to generate all the results are MATLAB (2021B) and Python 11.1. The code used in this study is available on Zenodo via https://zenodo.org/records/15869647 (ref. 76).

58. Hansen, M. C., Stehman, S. V. & Potapov, P. V. Quantification of global gross forest cover loss. *Proc. Natl Acad. Sci. USA* **107**, 8650 (2010).
59. Ferro, P. D. et al. Regional-scale assessment of burn scar mapping in southwestern Amazonia using burned area products and CBERS/WFI data cubes. *Fire* **7**, 67 (2024).
60. Pessôa, A. C. M. et al. Intercomparison of burned area products and its implication for carbon emission estimations in the Amazon. *Remote Sens.* **12**, 3864 (2020).
61. van Wees, D. et al. Global biomass burning fuel consumption and emissions at 500 m spatial resolution based on the Global Fire Emissions Database (GFED). *Geosci. Model Dev.* **15**, 8411–8437 (2022).
62. Potapov, P. et al. Mapping global forest canopy height through integration of GEDI and Landsat data. *Remote Sens. Environ.* **253**, 112165 (2021).
63. Santoro, M. & Cartus, O. ESA Biomass Climate Change Initiative (Biomass_cci): global datasets of forest above-ground biomass for the years 2010, 2017, 2018, 2019 and 2020, v4. *NERC EDS Centre for Environmental Data Analysis* https://doi.org/10.5285/af60720c1e404a9e9d2c145d2b2ead4e (2023).
64. Petersson, H. et al. Individual tree biomass equations or biomass expansion factors for assessment of carbon stock changes in living biomass—a comparative study. *For. Ecol. Manag.* **270**, 78–84 (2012).
65. Potapov, P. et al. The last frontiers of wilderness: tracking loss of intact forest landscapes from 2000 to 2013. *Sci. Adv.* **3**, e1600821 (2017).
66. Hartung, M., Carreño-Rocabado, G., Peña-Claros, M. & van der Sande, M. T. Tropical dry forest resilience to fire depends on fire frequency and climate. *Front. For. Glob. Change* **4**, 755104 (2021).
67. Nguyen, T. V. et al. Human-driven fire regime change in the seasonal tropical forests of central Vietnam. *Geophys. Res. Lett.* **50**, e2022GL100687 (2023).
68. Senf, C. & Seidl, R. Post-disturbance canopy recovery and the resilience of Europe's forests. *Glob. Ecol. Biogeogr.* **31**, 25–36 (2022).
69. Fawcett, D. et al. Declining Amazon biomass due to deforestation and subsequent degradation losses exceeding gains. *Glob. Change Biol.* **29**, 1106–1118 (2023).
70. Giardina, C. P. Advancing our understanding of woody debris in tropical forests. *Ecosystems* **22**, 1173–1175 (2019).
71. Harmon, M. E. et al. Release of coarse woody detritus-related carbon: a synthesis across forest biomes. *Carbon Balance Manag.* **15**, 1 (2020).
72. Zanne, A. E. et al. Termite sensitivity to temperature affects global wood decay rates. *Science* **377**, 1440–1444 (2022).
73. Parton, W. J., Stewart, J. W. B. & Cole, C. V. Dynamics of C, N, P and S in grassland soils: a model. *Biogeochemistry* **5**, 109–131 (1988).
74. Ometto, J. P. et al. A biomass map of the Brazilian Amazon from multisource remote sensing. *Sci. Data* **10**, 668 (2023).
75. Rodda, S. R. et al. LiDAR-based reference aboveground biomass maps for tropical forests of South Asia and Central Africa. *Sci. Data* **11**, 334 (2024).
76. Xu, Y. Small persistent clearings in humid forests drive tropical forest biomass carbon losses. *Zenodo* https://doi.org/10.5281/zenodo.15869647 (2025).

Acknowledgements W.L. acknowledges the support from the Yunnan Provincial Science and Technology Project at Southwest United Graduate School (202302AO370001). P.C., Y.X. and W.L. acknowledge the support from the CALIPSO (Carbon Loss in Plant Soils and Oceans) project funded through the generosity of Schmidt Science. P.C. and Y.X. thank the support from the European Space Agency Climate Change Initiative (ESA-CCI) RECCAP2-CS project (ESA ESRIN/4000144908/24/I-LR). J.C. is supported by projects ANR-10-LABX-0041 and ANR-21-CE32-0009. S.P.K.B. acknowledges support from the ESA-CCI cross-essential climate variables project XFires (ESA grant 4000145351). This work was also supported by the ESA-CCI Biomass project (ESA ESRIN/4000123662/18/I-NB), the French National Research Agency (ANR) under the French–German AI4Forest project (ANR-22-FAI1-0002-01), and the One Forest Vision initiative funded by the French Ministry of Higher Education and Research and the French Ministry for Europe and Foreign Affairs.

Author contributions Y.X., P.C. and W.L. designed the research. Y.X. collected and processed the data and constructed the figures and tables with contributions from P.C., F.R., A.P.-T., Y.F., C.Z., S.B., V.H., S.C.C.-P., C.B., Y.S. and W.L. M.S., C.B., G.H., J.P.O and J.-P.W. contributed to data acquisition. M.S., C.B., N.R., J.C., L.E.O.C.A., S.P.K.B., I.F. and L.Z. contributed to the interpretation of the data and results. Y.X. drafted the paper, and all authors contributed to revising and improving the text.

Competing interests The authors declare no competing interests.

Additional information

Supplementary information The online version contains supplementary material available at https://doi.org/10.1038/s41586-025-09870-7.

Correspondence and requests for materials should be addressed to Philippe Ciais or Wei Li.

Peer review information *Nature* thanks Ricardo Dalagnol, Félicien Meunier and the other, anonymous, reviewer(s) for their contribution to the peer review of this work.

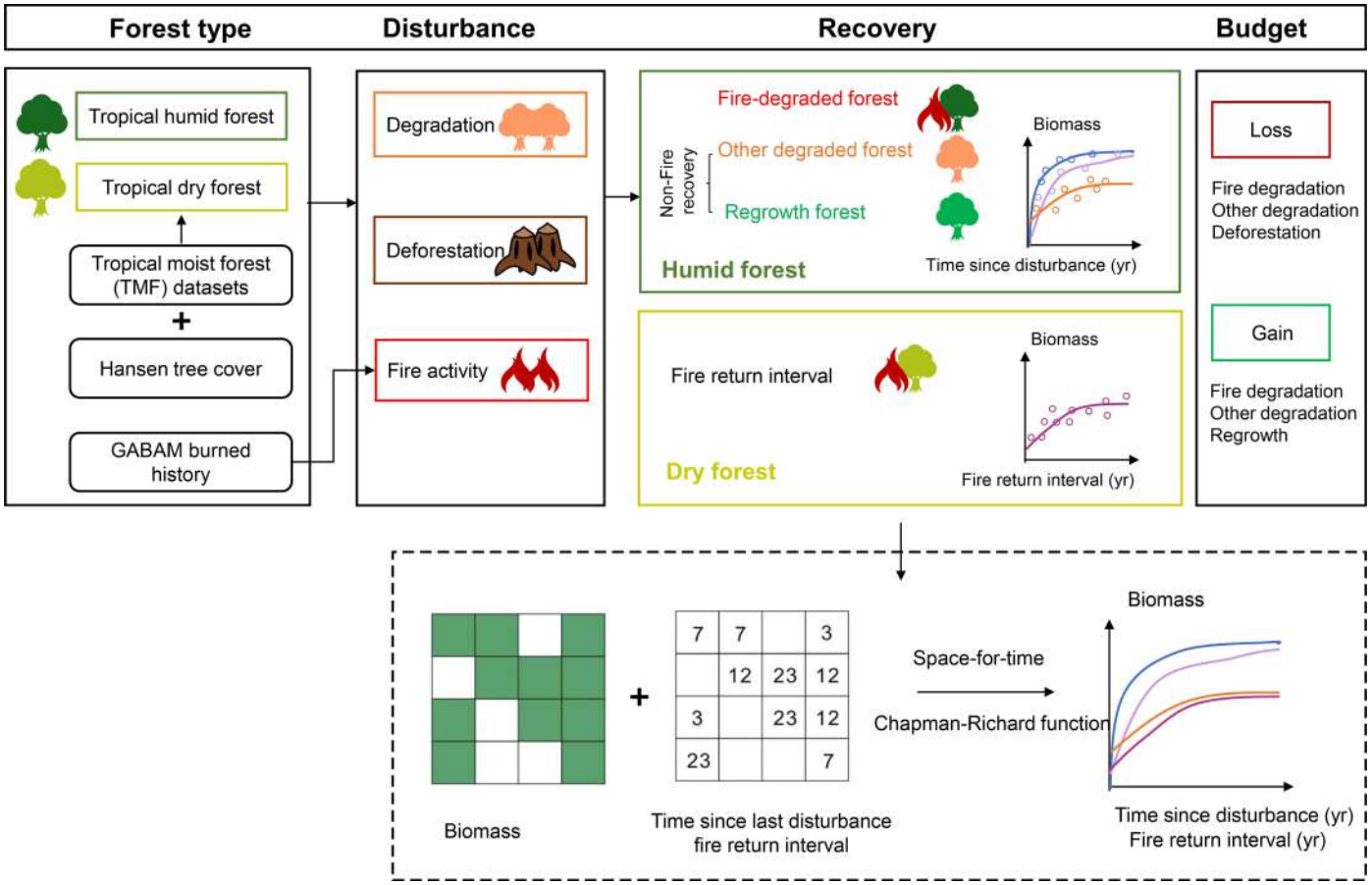

Extended Data Fig. 1 | Workflow of the new bookkeeping model with spatially-explicit recovery curves. (1) Categorization of tropical forests: Differentiation of dry and humid tropical forests. (2) Identification of disturbances: Separation of various types of disturbances, including fire-driven degradation, other degradation, deforestation, and the regrowth from newly established forests and regrowth from deforestation by combining different disturbance datasets; (3) Reconstruction of forest recovery: Derivation of forest biomass recovery curves for each 1° grid by combining the biomass and disturbance datasets; (4) Carbon budget calculation: Estimation of above-ground carbon (AGC) losses and subsequent gains for each disturbance event from 1990 to 2020. Icons adapted from Pixabay (https:/pixabay.com) under a Creative Commons licence CC0.

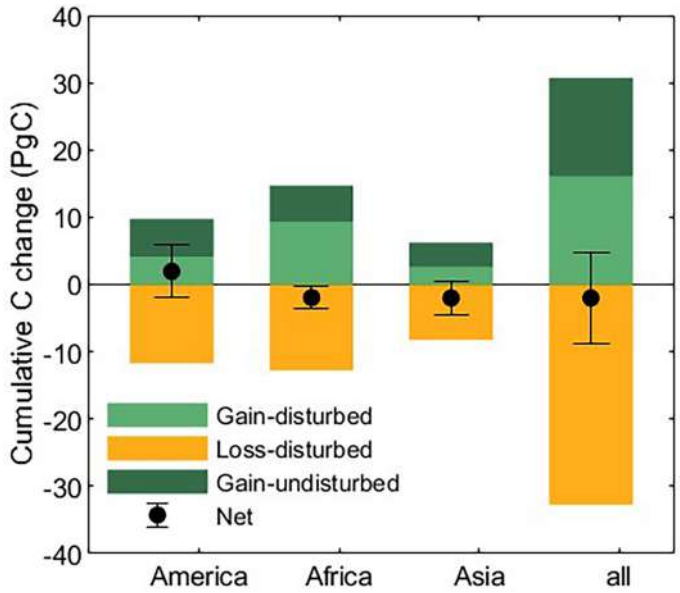

Extended Data Fig. 2 | Cumulative AGC changes in disturbed and undisturbed tropical forests during 1990–2020. Net AGC balance is calculated as the sum of gross AGC gains from disturbed and undisturbed forests and gross AGC losses from the disturbed forests. Black dots represent the net AGC changes (sum of all gains and losses) and the error bars represent the standard errors across each tropical region.

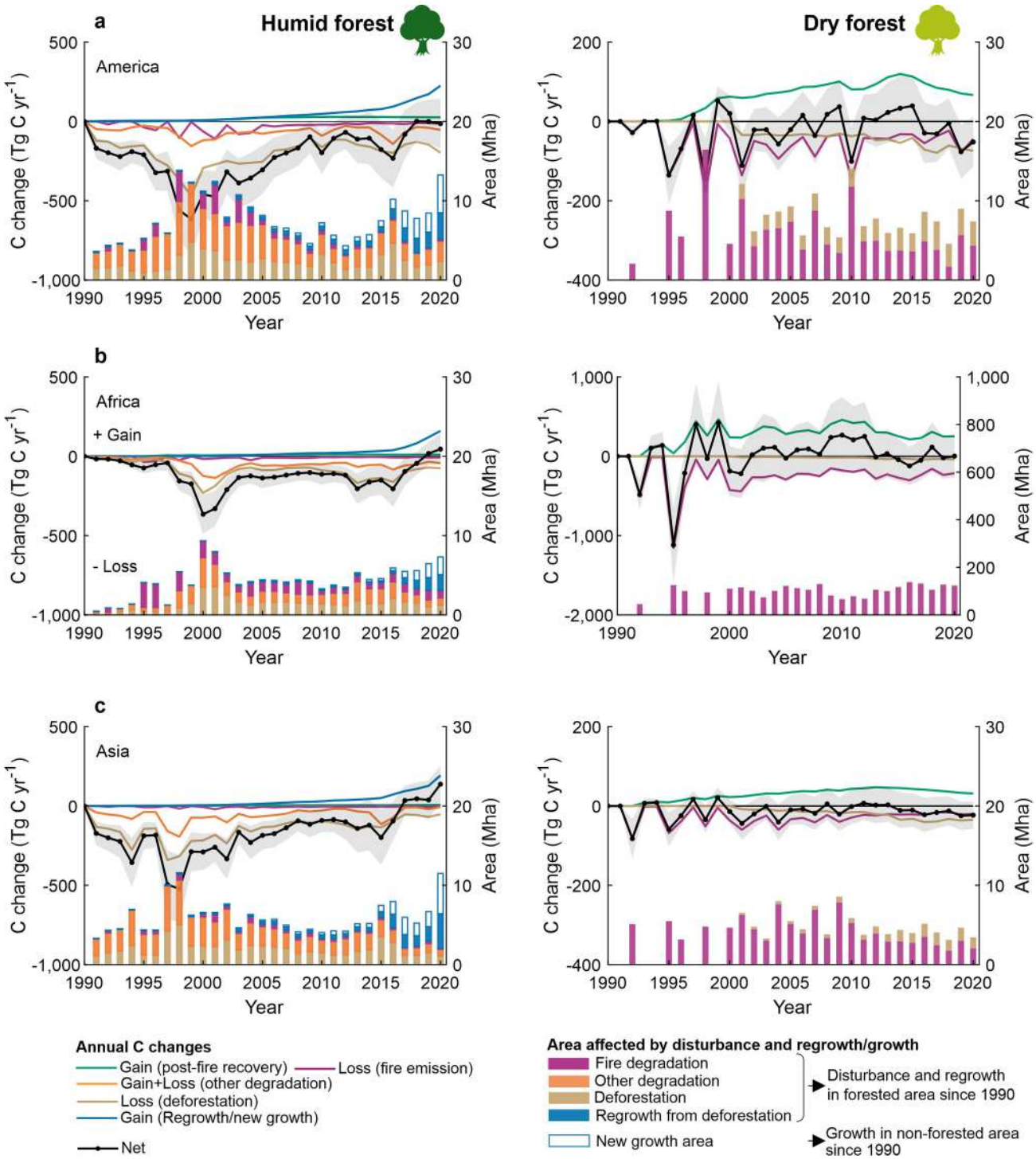

Extended Data Fig. 3 | Temporal dynamics of the forest AGC changes after disturbances in disturbed tropical humid and dry forests during 1990–2020. a) Tropical forests in Africa, b) America, and c) Asia. Black lines and shaded areas represent the annual net C balance by summing up all the C flux components and the corresponding standard errors. The bars represent the annual disturbed area associated with different types of disturbances. Due to the limited availability of Landsat data, there is a 5-year lacuna of burned areas in the 1990s. Icons adapted from Pixabay (https:/pixabay.com) under a Creative Commons licence CC0.

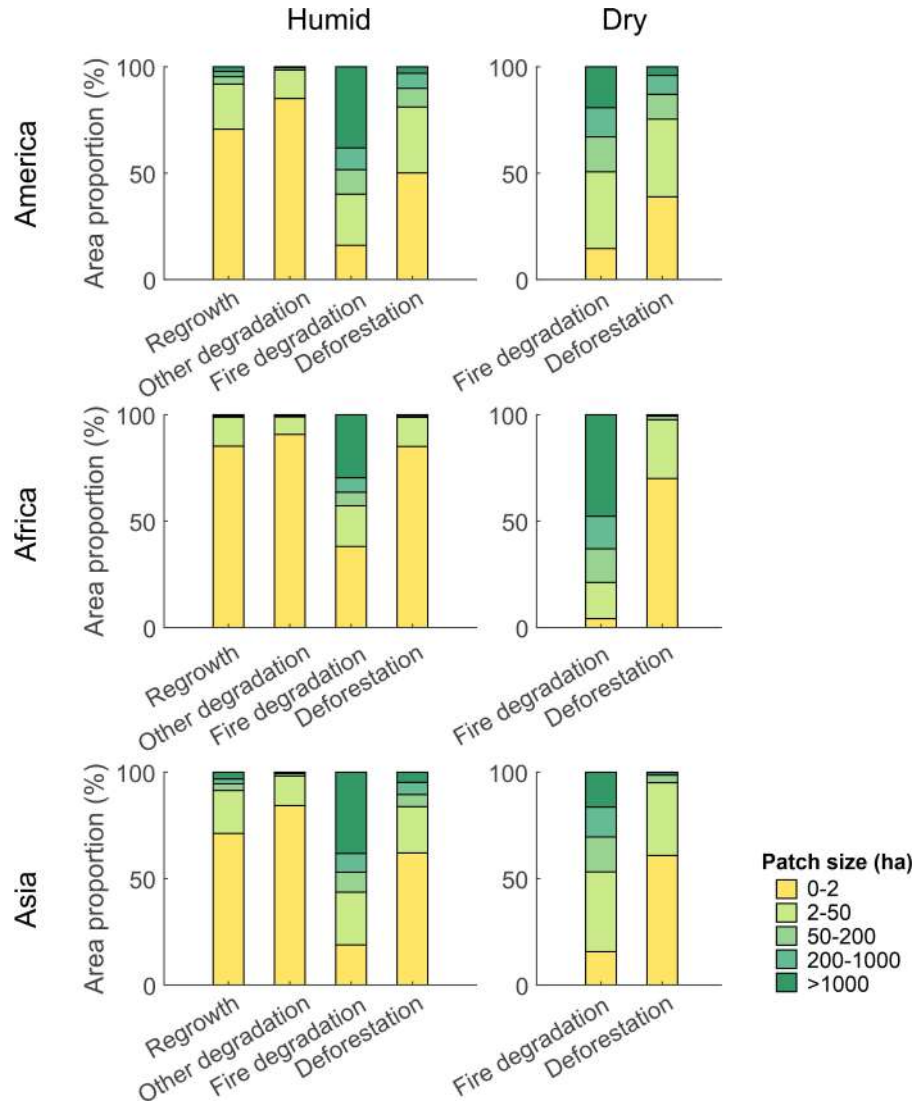

Extended Data Fig. 4 | Area proportion of tropical forest disturbance types by patch size. Bars represent the cumulative contribution of different disturbance patch sizes aggregated over the period from 1990 to 2020.

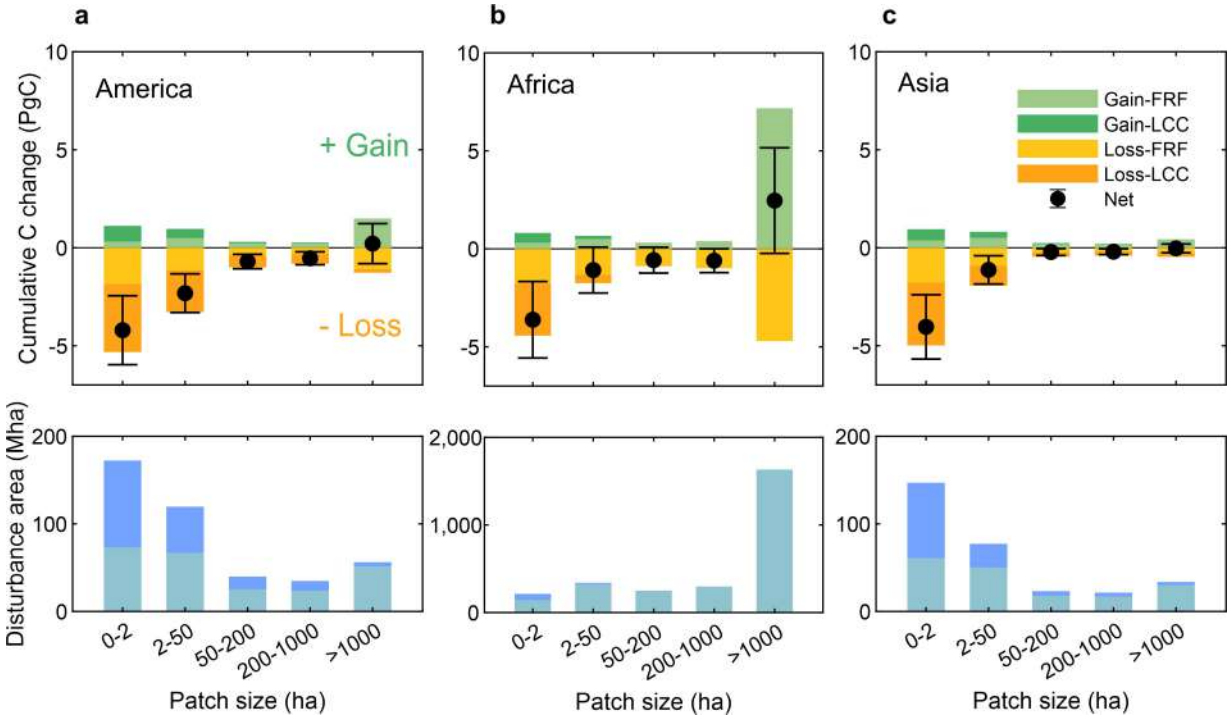

Extended Data Fig. 5 | Gross and net C changes contributed by disturbances from different size classes during 1990–2020 across tropical regions. Tropical a) America, b) Africa, and c) Asia. Black dots and error bars represent the net C balance and the corresponding standard errors for each disturbance patch size class. The C losses, gains, and area changes are separated into FRF and LCC categories. FRF: disturbances occurring within the remaining forest, such as fire-driven degradation and other degradation. LCC: disturbances associated with forest land cover change (permanent or temporary), such as deforestation or afforestation. Positive values indicate a C gains, and negative values indicate a C losses.

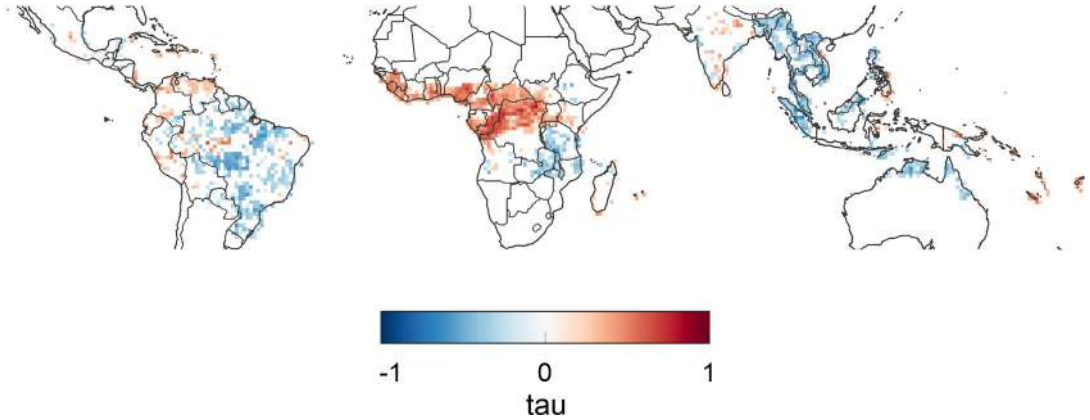

Extended Data Fig. 6 | Trend in forest fire frequency during 1990–2020 based on Kendall's tau. Kendall's correlation tau is calculated based on the annual forest burned area during 1990–2020 across each 1° grid cell from[16]. *tau* values close to +1 suggest a strong increase in fire frequency, while tau values close to −1 indicate a strong downward trend in fire frequency. Only grid cells with statistically significant trends (p-value ≤ 0.05) are shown. Administrative boundaries adapted from data © European Union, 1995–2025.

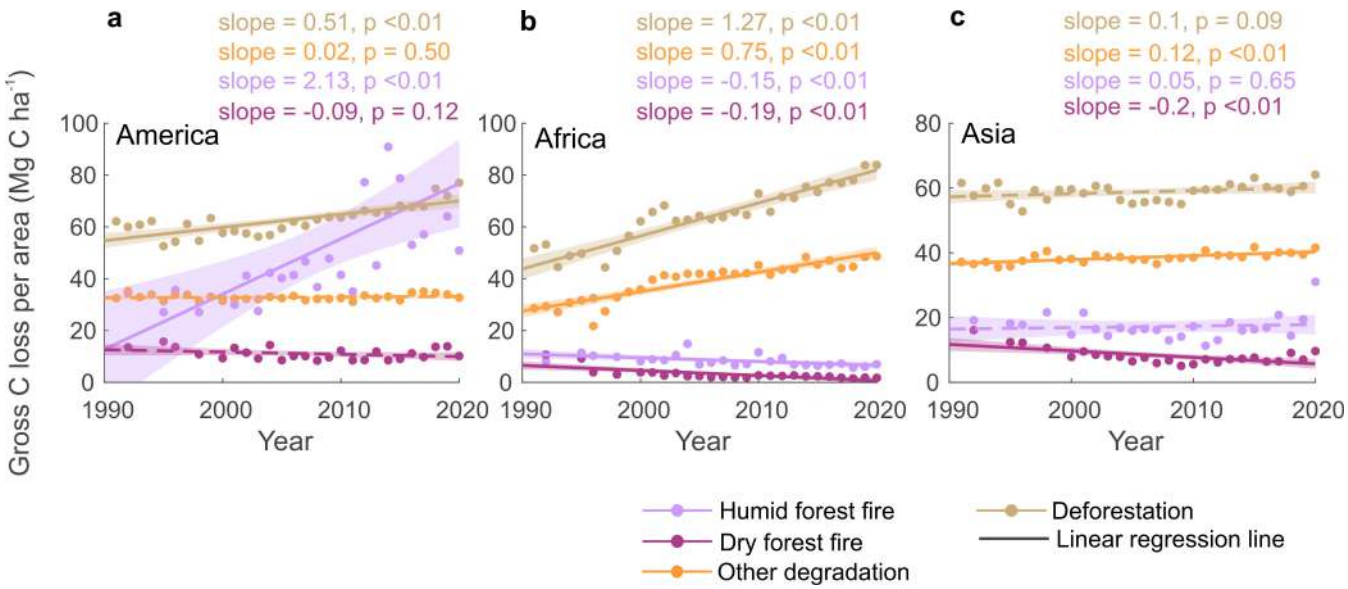

Extended Data Fig. 7 | Temporal changes of gross forest AGC loss per unit of disturbed forest area caused by different types of disturbance from 1990 to 2020. Tropical forests in a) America, b) Africa, and c) Asia. Solid lines indicate statistically significant trends (linear regression, slope t-test, $p < 0.01$), while dashed lines represent non-significant trends.

Extended Data Table 1 | Definition and data source of disturbance types described in this study

Disturbance category	sub-category	Dataset source and method	Group	W(with)/O (without) Recovery	Partial or full clearing
Fire-driven degradation		Degradation fires in the humid domain were identified by the fire records from GABAM, overlapping with humid forest extent and excluding the deforested areas from TMF. Fires in the dry domain were attributed by overlapping the dry forest extent with the fire records from GABAM. Additional thresholds of canopy height in 2019 taller than 5m were used to ensure only forests with the signal of forest recovery were included in this category.	FRF	W	Partial
Other degradation		The remaining degraded forest was identified from TMF. Fire-degraded forests are excluded.	FRF	W	Partial
Deforestation		Deforested forest identified from TMF for humid forest extent; GFW tree cover loss after removing the tree cover gain for dry forest extent. When fire overlaps with deforestation (deforestation fire), it is counted in the deforestation category.	LCC	O	Full
Regrowth	newly established forests	Regrowth forest identified from TMF. Including 1) forests regenerating from deforestation and 2) forests newly established from non-forested land based on the existing forest extent and 31-year deforestation records	LCC	W	/
	regenerating forests from deforestation				

All these disturbances are classified into two groups 1) Forest remains forest (FRF) indicates disturbances occuring within forest remaining forest, such as fire, logging, and windthrows which induce a reduction of forest biomass but do not cause a shift in forest land cover type. 2) Disturbance associated with forest land cover change (LCC) (permanent or temporary) such as deforestation, forest regrowing from deforested land or new forest established on previously non-forested land.